JGR Oceans

RESEARCH ARTICLE
10.1029/2020JC016131

Key Points:
- The internal vertical exchange in response to the external flux is crucial to the layered circulation in the South China Sea
- The vertical exchange through vortex stretching and squeezing modulates layered circulation in the semi-closed middle and deep layers
- The study advanced the understanding of the intrinsic-extrinsic dynamic coupling that forms, develops, and sustains the layered circulation

Correspondence to:
J. Gan,
magan@ust.hk

Citation:
Cai, Z., & Gan, J. (2020). Dynamics of the cross-layer exchange for the layered circulation in the South China Sea. *Journal of Geophysical Research: Oceans*, *124*, e2020JC016131. https://doi.org/10.1029/2020JC016131

Received 31 JAN 2020
Accepted 26 JUN 2020
Accepted article online 1 JUL 2020

Dynamics of the Cross-Layer Exchange for the Layered Circulation in the South China Sea

Zhongya Cai[1,2] and Jianping Gan[1]

[1]Department of Ocean Science and Department of Mathematics, The Hong Kong University of Science and Technology, Hong Kong, [2]State Key Laboratory of Internet of Things for Smart City and Department of Civil and Environmental Engineering, University of Macau, Macau

Abstract The cyclonic-anticyclonic-cyclonic (CAC) circulation in the upper (<750 m)-middle (750–1,500 m)-deep (>1,500 m) layers of South China Sea (SCS) is mainly driven by the extrinsic lateral vorticity flux due to inflow-outflow-inflow through the Luzon Strait (LS) and the associated intrinsic vertical exchange (VE) in the basin. The contribution of spatiotemporal structure of the VE through vortex stretching and squeezing to CAC circulation, which was unknown, mainly occurs in the semi-closed middle and deep layers and has a strong seasonality. During summer, the vorticity flux induced by net upward VEs crossing the upper (750 m) and lower (1,500 m) interfaces of CAC circulation is equivalent to ~40% of the lateral vorticity flux for strengthening the anticyclonic and cyclonic circulation in the middle and deep layers, respectively. During winter, the net downward VE crossing the upper interface squeezes the middle layer and strengthens its anticyclonic circulation, while the net VE crossing the lower interface is too small to affect the circulation. The VE and its seasonality in the basin are largely governed by the cross-isobath geostrophic transport (CGT_b) due to interaction between along-isobath circular currents and rugged slope topography. The CGT_b is formed by the along-isobath bottom pressure gradient associated with surface wind stress curl, nonlinear advection, and beta effect over the meandering slope topography. Our study revealed how important VE between the layers is to the CAC circulation itself, and our work advanced the understanding of the intrinsic-extrinsic dynamic coupling that forms, develops, and sustains the CAC circulation in the SCS.

1. Introduction

The South China Sea (SCS) is the largest marginal sea in the tropics (Figure 1). It has a deep basin, a shallow broad shelf on its northern and southern sides, and a steep continental slope in the east and west. The SCS connects to the East China Sea through the Taiwan Strait, to the Pacific Ocean through the Luzon Strait (LS), to the Sulu Sea through the Mindoro Strait (MS), and to the Java Sea through the Karimata Strait. Only LS, which is the deep channel (~2,500 m deep), connects the deep SCS to the open Pacific Ocean, and the three other straits are much shallower than LS. The maximum water depth of the deep SCS basin is over 4,000 m, and the deep basin is enclosed below ~2,500 m. The deep center basin of the SCS orients southwest to northeast, and it is surrounded by shelf and slope regions between the 200 and 3,000 m isobaths.

The SCS has a layered circulation (Gan, Liu, & Hui, 2016; Gan, Liu, & Liang, 2016; Xu & Oey, 2014; Yuan, 2002; Zhu et al., 2019) that is driven by the seasonal Asian monsoon and the Kuroshio intrusion through LS (Fang et al., 2009; Gan et al., 2006; Qu, 2000; Qu et al., 2009; Su, 2004; Xue et al., 2004). In the upper layer in winter, the circulation is cyclonic with a southwestward current along the continental margin in the northern and western parts of the basin. In summer, the upper circulation is cyclonic/anticyclonic in the northern/southern half of the basin (Qu, 2000). In the enclosed deeper ocean, the circulation is cyclonic (Lan et al., 2013, 2015; G. Wang et al., 2011). Gan, Liu, and Hui (2016) and Gan, Liu, and Liang (2016) defined the three-layer cyclonic-anticyclonic-cyclonic (CAC) circulation in geopotential level under the principle of the Stokes Theorem (Cai et al., 2020). Three layers are separated at the depths of 750 and 1,500 m (Figure 1).

The CAC circulation in the SCS basin is dynamically related to external forcing coming through the straits on the periphery of SCS (Gan, Liu, & Hui, 2016; Lan et al., 2013; Yang & Price, 2000, 2007; Zhu et al., 2017). The sandwich-like inflow-outflow-inflow through the upper-middle-lower layers of LS (e.g., Chen &

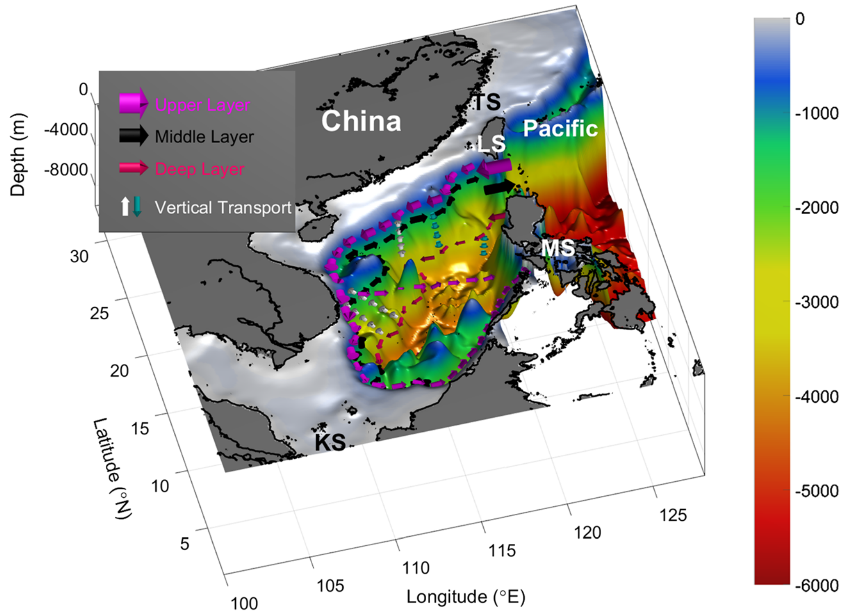

Figure 1. Schematic annual mean CAC circulation in the South China Sea. Color contours represent bathymetry (m). The white and green arrows indicate the upward and downward transport in CAC circulation. LS = Luzon Strait; TS = Taiwan Strait; MS = Mindoro Strait; and KS = Karimata Strait.

Huang, 1996; Hsin et al., 2012; Tian et al., 2006; Xu & Oey, 2014) provides the positive-negative-positive planetary vorticity for the CAC circulation in the three layers, respectively.

Although the external forcing of lateral vorticity flux largely controls the overall basin-scale circulation, the internal vertical motion can induce positive/negative vorticity through vortex stretching/squeezing to establish vertical coupling between two adjacent layers. In classic Stommel-Arons theory (Stommel & Arons, 1960), the uniform vertical motion maintains the abyssal circulation, and the spatial distribution of the vertical flux changes the abyssal circulation pattern (e.g., Katsman, 2006; Marchal & Nycander, 2004). Following Luyten and Stommel (1986), Wang et al. (2012) found that upwelling from the base of a layer could induce anticyclonic circulation (negative vorticity) in a layer. Similarly, Wang et al. (2018) showed that downwelling occurring in the interior basin of the SCS could broaden the deep circulation and create a southward current. Using a three-layer model, Quan and Xue (2018) illustrated that the layer thickness variation, which represents the vertical motion in a geopotential coordinate system, is the key to linking the upper and middle layers and to regulating the variability of the SCS basin circulation. Based on the process-oriented numerical modeling, Cai and Gan (2019) proposed that the vertical vorticity flux associated with the divergence/convergence of water ($-f\nabla \cdot \vec{V}_h$) plays a significant role in the vorticity balance in the semi-closed middle and lower layers, which dynamically links the CAC circulation in the different layers and sustains the layered circulation.

In the end, however, the earlier studies mainly considered a one-way influence between two layers, or they were based on simplified physics. The complete dynamic processes within the CAC circulation, particularly regarding interaction or coupling among the circulation in the different layers, have not been well investigated. Recently, Liu and Gan (2017) explored the three-dimensional "pathway" of the water inside the SCS, but they did not illustrate the effect of the three-dimensional motion on the CAC circulation. So far, knowledge of the spatiotemporal vertical coupling in the CAC circulation is limited, but knowing how the coupling is crucial to understanding how the layered circulation in the SCS is formed and sustained. In this paper, we examine the three-dimensional structure and seasonal variability of the vertical exchange (VE) across the upper (750 m) and lower (1,500 m) interfaces that separate the three layers of the CAC circulation and explore dynamics of vertical coupling in the CAC circulation.

2. The Numerical Model and Methods

We used results from the China Sea Multi-scale Ocean Modeling System (CMOMS, https://odmp.ust.hk/cmoms/) (Gan, Liu, & Liang, 2016) for our study. The modeling system is based on the Regional Ocean Modeling System (ROMS) (Shchepetkin & McWilliams, 2005). The model domain covers the North Pacific Ocean and the China Seas from approximately 0.958°N, 99.8°E in the southwest to the northeast corner of the Sea of Japan. The domain has a horizontal resolution of about 0.18°, and there are 30 levels over the stretched terrain following coordinates. Fluxes from a larger-scale global model, the Ocean General Circulation Model for the Earth Simulator (OFES) (Masumoto et al., 2004), provided the external flux along the open boundaries of CMOMS, which included both tidal and subtidal forcing using the novel open boundary condition of Liu and Gan (2016). CMOMS was initialized with the WOA13 (World Ocean Atlas) hydrographic field and spun up for 50 years with climatological atmospheric and lateral fluxes until it reached a quasi-steady state. For this study, we used an average of the last 5 years of runs. CMOMS results were validated rigorously with field measurements, satellite remote sensing data, and principles of geophysical fluid dynamics (Gan, Liu, & Hui, 2016; Gan, Liu, & Liang, 2016; Liu & Gan, 2017). The fact that the model realistically captures the circulation and forcing conditions in the SCS establishes a level of confidence in the results that we used. The detailed description and validation of CMOMS can be found in Gan, Liu, and Hui (2016) and Gan, Liu, and Liang (2016).

The contribution of vertical motion to vorticity change in the CAC circulation can be illustrated by layer-integrated vorticity dynamics (Cai & Gan, 2019; Gan, Liu, & Hui, 2016),

$$\nabla \times \int_{L_b}^{L_u} \frac{\partial \vec{V}_h}{\partial t} dz = \nabla \times \underbrace{\int_{L_b}^{L_u} -\vec{V} \cdot \nabla \vec{V}_h dz}_{\text{ADV}} + \nabla \times \int_{L_b}^{L_u} \underbrace{\frac{-1}{\rho_0} \nabla_h P}_{\text{PGF}} dz - \nabla \cdot \int_{L_b}^{L_u} f \vec{V}_h dz + \nabla \times \int_{L_b}^{L_u} \underbrace{\left[K_v \left(\vec{V}_h \right)_z \right]_z}_{\text{VVIS}} dz, \tag{1}$$

where L_u and L_b are the geopotential depths at the top and bottom of each of the three layers. $\vec{V}$ is the velocity vector, $\vec{V_h}$ is the horizontal velocity vector, and v is the velocity in the meridional direction. P is the pressure, f is the Coriolis parameter, and K_v is the vertical viscous coefficient. ADV, PGF, and VVSI represent the nonlinear advection, pressure gradient force, and vertical viscous terms, respectively. The contribution from horizontal viscous term is negligible.

In Equation 1, $-\nabla \cdot \int_{L_b}^{L_u} f \vec{V}_h dz$ links to the external planetary vorticity flux through the straits and can be further divided into $-f \nabla \cdot \int_{L_b}^{L_u} \vec{V}_h dz$ and $-\beta \int_{L_b}^{L_u} v dz$. The first part is the vortex stretching induced by the divergence/convergence of water, and the second part is the β effect of the meridional motion, where β is the meridional gradient of f. The integral, $-f \nabla \cdot \int_{L_b}^{L_u} \vec{V}_h dz$, is critical to the exchange of momentum and vorticity between two layers for the development and sustenance of the CAC circulation. Mathematically, the integral equals $f w_{L_u} - f w_{L_b}$, which represents the net vertical planetary vorticity flux across the upper and lower boundaries of a layer. Thus, the upward transport crossing the upper/lower boundary of a specific layer induces positive/negative vorticity in that layer by stretching/squeezing the layer, and vice versa.

Following Equation 1, we defined the VE at a depth, z:

$$VE(z) = -\nabla_h \cdot \int_{-H}^{z} \vec{V_h} dz, \tag{2}$$

where H is the bottom depth. The positive/negative VE indicates the upward/downward motion, respectively. The VE links to the inhomogeneous horizontal circulation and the external lateral transport through the straits (mainly LS), and we used VE to diagnose the budget of the momentum and vorticity in the different layers. A similar method was used in previous studies, for example, Liang et al. (2017). We integrated Equation 2 within the respective layers in the CAC circulation, obtained spatial variation of VEs across the two interfaces that separate the three-layer CAC circulation, and examined the effect of VE on the layered circulation.

3. Results

3.1. Variability of CAC Circulation and VE

We examined the dynamic links between the large-scale CAC circulation, as illustrated by the transport stream function, and the corresponding VE in summer (June to August) (Figure 2) and winter (December to February) (Figure 3). We focused on the net VE crossing the upper (750 m) interface that separates the upper and middle layers and the net VE crossing lower (1,500 m) interface that separates the middle and deep layers. The depths of two interfaces and the associated VEs across them in the basin match with depths of inflow-outflow-inflow volume fluxes through the LS according to mass conversation, and they represent the vertical flux across the neighboring layers in the CAC circulation.

3.1.1. Upper Layer

Surface wind forcing and the external Kuroshio intrusion drove the basin circulation in the upper layer. During summer, in the northern SCS (north of 13°N) (Figure 2a), the water entered the basin through LS and flowed cyclonically along the slope around the basin. The slope current intensified and flowed over the relatively steep and narrow western slope. This southward current flowed from the northern SCS and converged with the northward western boundary current from the southern SCS (south of 13°N) (Gan & Qu, 2008). Together, they formed an eastward current toward MS along ~13°N.

At the upper interface (750 m), the VE varied over the basin. Relatively strong VE occurred mainly along the slope (Figure 2d) due to the slope current interacting with the meandering bottom topography (Gan et al., 2013). The upslope (positive) and downslope (negative) motions alternated along the slope (Figure 2d) as the slope currents encountered respective convex and concave isobaths over the slope (Gan & Allen, 2002; Song & Chao, 2004). In the southern basin (south of the 10°N and the 3,000 m isobath line), VE was generally positive. When averaged over the basin, VE at the interface between the upper and middle layers was positive, which we expected to weaken the circulation in the upper and middle layers.

During winter, the intruding Kuroshio and positive wind stress curl enhanced, which strengthened the cyclonic circulation in the upper layer, particularly along the western slope (Figure 3a). The basic pattern of the winter VE remained like the summer VE characteristics except the magnitude of the VE varied more in winter.

3.1.2. Middle and Deep Layers

In the semi-closed middle layer (Figures 2b and 3b), the basin anticyclonic circulation was mainly contributed by the strong northward boundary current over the steep western slope, while a cyclonic eddy circulation in the north-eastern basin was largely influenced by the inflow/outflow through the northern/southern portion of the LS. Over the southern basin, the current contributed relatively less to the overall basin circulation. Like in the upper layer, the cyclonic circulation intensified over the basin along the western slope during winter.

At the lower interface (1,500 m), in response to the spatial variation of the circulation, the upward VE crossing the lower interface (1,500 m) occurred along the meandering steep and narrow basin slope (Figure 2e), just like the VE that crossed the upper interface (Figure 2d). However, the VE that crossed at 1,500 m was stronger than the VE that crossed at 750 m. In the north-eastern basin, there was an upward and downward VE in and around the cyclonic eddy circulation. Compared to VE at the upper interface, the total positive VE was stronger at the lower interface. From summer to winter, the upward/downward VE was reduced/intensified over both the northern basin and western slope.

Overall, there was a net upward motion crossing the upper and lower interfaces, which induces negative vorticity by squeezing the middle layer to modulate the intensity of the anticyclonic circulation, particularly over the steep western slope. The basin-integrated effect of VE crossing the two interfaces determined the integrated net VE in the middle layer, as to be shown below.

In the deep layer, the cyclonic circulation was mainly contributed by the circulation in the northern and southwestern basin (Figure 2c). The VE crossing the lower interface strengthened the circulation in the deep and middle layers by providing positive and negative vorticity through stretching and squeezing (Figure 2e), respectively. Seasonally, the deep cyclonic circulation weakened due to a reduced deep intrusion during winter (Gan, Liu, & Hui, 2016), so did the upward motion crossing the lower interface at 1,500 m (Figures 3c and 3e).

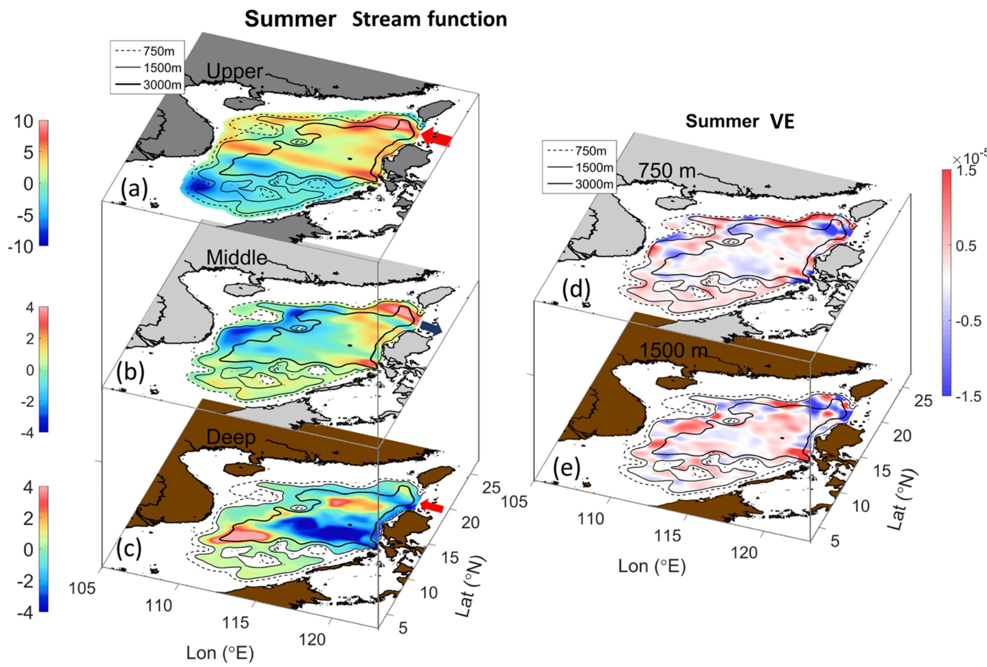

Figure 2. (a–c) Transport stream function (color contours, Sv) integrated over the upper (<750 m), middle (750–1,500 m), and deep layers (>1,500 m) in summer. The region over the continental shelf shallower than 200 m is excluded. (d, e) Horizontal map of VE (color contour, m/s) across the upper interface (750 m) and lower interface (1,500 m) in summer.

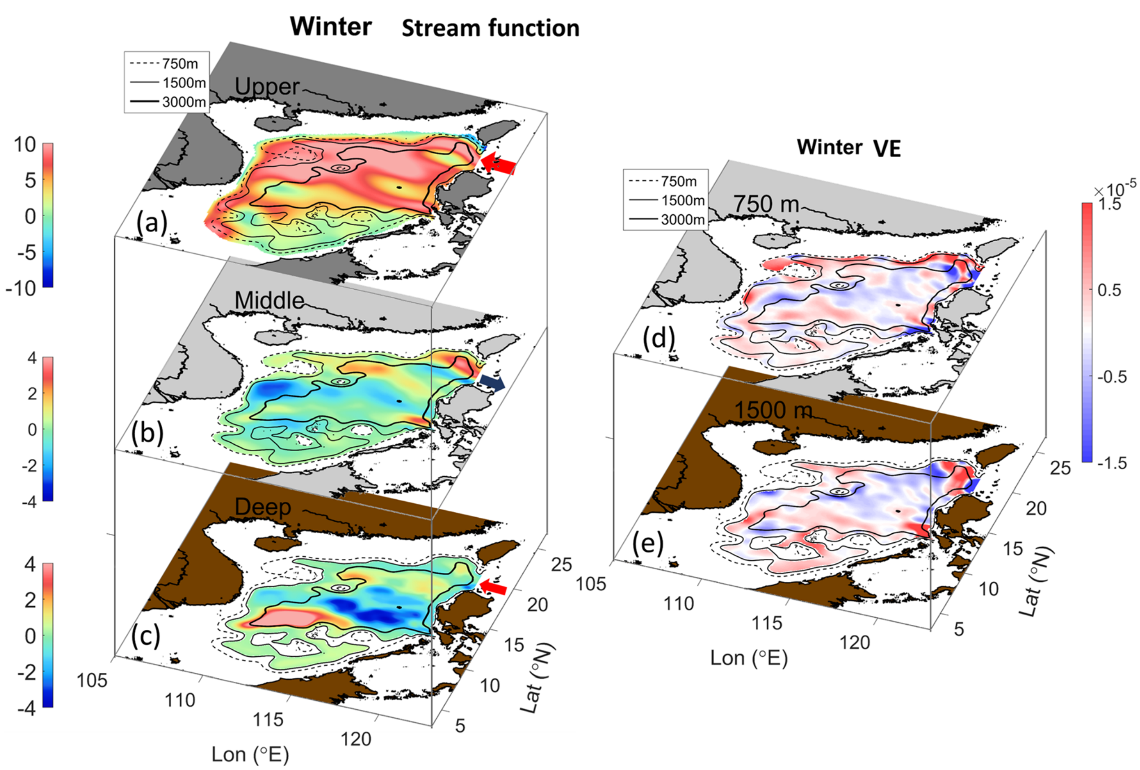

Figure 3. Same as Figure 2, but for winter.

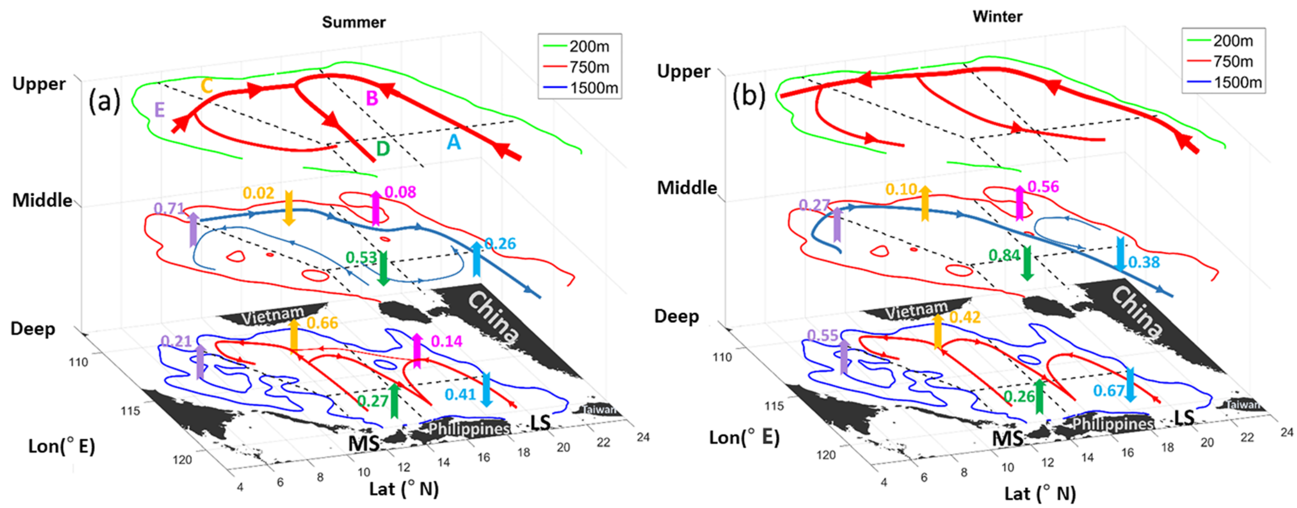

Figure 4. The CAC circulation pattern and net VE transport (Sv) among three layers in five regions (A–E) during (a) summer and (b) winter. Green, red, and blue lines represent three isobath lines. The vertical arrows in different colors indicate the VE transport across the upper (750 m) and lower (1,500 m) interfaces in the five regions. The solid red and blue lines with arrows are the transport trajectories in the upper, middle, and deep layers, schematically derived from the stream function in Figures 2 and 3. Thicker lines represent stronger transports.

3.2. Quantitative Cross-Layer VE

To better quantify the variability of VE associated with the circulation pattern over the basin, we calculated VE in five subdomains (Figure 4): Region A near LS, Region B in the north-western basin with the meandering slope, Region C in the western and southwestern basin with the steep slope, Region D near MS, and Region E in the southern basin. We connected the horizontal transport of the CAC circulation in the basin to the VE across the upper and lower interfaces, particularly in the deep and middle layers where the influence of VE on basin circulation was relatively strong over the semi-closed basin (Figures 2 and 3).

At the upper interface (Figures 4a and 4b), the upward motion occurred in Regions E and A with a total VE of 0.97 Sv during summer and in Regions E and B with a total VE of 0.83 Sv during winter. The downward motion occurred near MS (−0.53 Sv) during summer and near LS and MS with a total VE of −1.22 Sv during winter. Over the meandering western slope of Region C, the upward motion (−0.02 Sv in summer and 0.10 Sv in winter) was generally much weaker at the upper interface than at the lower interface, and the anticyclonic current in the middle layer prevailed along the slope. However, a stronger upward motion at the upper interface (than that at the lower interface) still existed in the regions with a locally intensified cyclonic flow in the middle layer.

Overall, at the upper interface, there was a net upward transport of 0.50 Sv during summer, but a net downward transport of 0.29 Sv during winter, which weakened and strengthened the cyclonic circulation in the upper layer, respectively. Similarly, VE crossing this interface weakened and strengthened the anticyclonic circulation in the middle layer during summer and winter, respectively.

At the lower interface, some of the deep intruding water sunk to the abyssal SCS after entering the basin near LS. Then the deep inflow flowed southwestward along the slope in the northern basin and formed a distinct eddy-like cyclonic circulation over the southwest corner. This cyclonic along-slope current in the deep layer generated an upslope VE across the lower interface along the meandering slope topography. The upslope VE was distinctly larger along the steep western slope in Regions B and C with a total transport of 0.80 Sv in summer and 0.42 Sv in winter. In Region E, over the southern basin, the upward VE was relatively weak in summer (0.21 Sv) and intensified in winter (0.55 Sv). Overall, there was a net upward VE (0.87 Sv in summer and 0.56 Sv in winter) crossing the lower interface, which was stronger during summer with a larger influx through the LS. The upward VE crossing the lower interface tended to strengthen the cyclonic flow in the deep layer. It could have also enhanced the anticyclonic circulation in the middle layer if the net VE across the upper interface was also favorable. The transport provided by the VE produced vertical vorticity flux in each layer to maintain the CAC circulation.

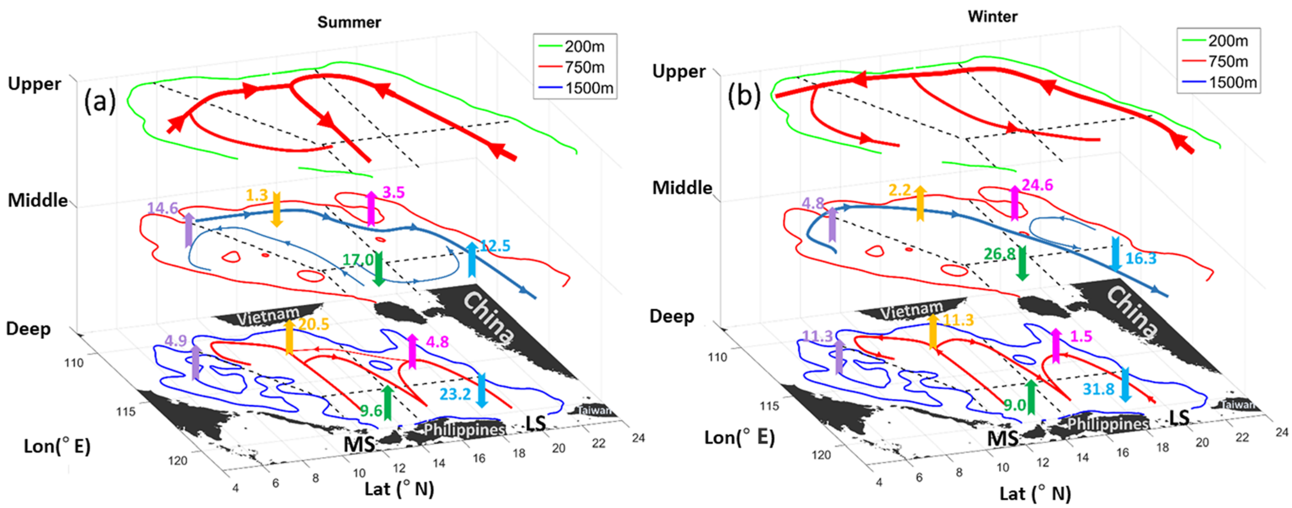

Figure 5. Same as Figure 4, but for the horizontal CAC circulation pattern and vertical vorticity flux (vertical arrows, m^3/s^2).

3.3. Vertical Vorticity Flux

The VE across the upper and lower interfaces produced vertical vorticity flux in each layer and contributed to the layered circulation adjacent to the interfaces (Figure 5), particularly in the semi-closed middle and deep layers. The upward transport crossing the upper/lower boundary of a specific layer could have induced positive/negative vorticity in that layer by stretching/squeezing the layer, and vice versa. Although the basic structure of the vertical vorticity flux was similar to the VE structure, the vertical vorticity flux magnitude varied due to the meridional changes of the Coriolis parameter, f, and the VE contributed relatively more/less to the CAC circulation in the northern/southern part of the basin (Figure 5).

At the upper interface (Figures 5a and 5b), the upward vorticity flux occurred in Regions A and E with a total flux of 27.1 m^3/s^2 during summer, while the upward flux was mainly in Region B (24.6 m^3/s^2) during winter. The downward vorticity flux was near MS (−17.0 m^3/s^2) in summer and near LS and MS in winter (−43.1 m^3/s^2). Combining the upward and downward vorticity fluxes, the net vertical vorticity flux crossing the upper interface was upward (12.3 m^3/s^2) in summer and changed to downward (−11.5 m^3/s^2) in winter.

At the lower interface, the cascading deep intruding water near LS had large f and generated a strong downward vorticity flux (−23.2 m^3/s^2 in summer and −31.8 m^3/s^2 in winter). Inside the basin, associated with the upslope VE along the meandering basin slope, the upward vorticity flux occurred over the western slope (Regions B and C) and southern basin (Region E) and had a total upward flux of 30 m^3/s^2 in summer and 24.1 m^3/s^2 in winter. Overall, the net vertical vorticity flux across the lower interface was upward with a stronger magnitude during summer (16.6 m^3/s^2) than winter (1.3 m^3/s^2), which maintained the deep/middle layer cyclonic/anticyclonic slope current.

Unlike the circulation in the upper/deep layer that was affected only by the vertical vorticity flux crossing the respective upper/lower interface, the vorticity fluxes crossing these two interfaces all affected the circulation in the middle layer. During summer, the prevailing upward vorticity flux across the upper interface was weaker than the flux that crossed the lower interface, which induced the net positive vorticity input for cyclonic circulation in the deep layer and net negative vorticity input for anticyclonic circulation in the middle layer (Figure 6). Quantitatively, the vertical vorticity flux contributed little to the upper layer and was equivalent to ~10% of the magnitude of the external planetary vorticity flux induced by the Kuroshio intrusion. In contrast, the contribution of the net vertical vorticity flux to the circulation in the semi-closed middle and deep layers had a magnitude about 40% of the total external planetary vorticity flux through LS.

During winter, the contribution of the downward vertical vorticity flux crossing the upper interface was still about 40% of the external planetary vorticity flux to the circulation in the middle layer, which, however, had a much smaller influence on the upper layer vorticity input (~3%) (Figure 6). Unlike in summer, the magnitude of the vertical vorticity flux crossing the lower interface was small because the intensified downward VE

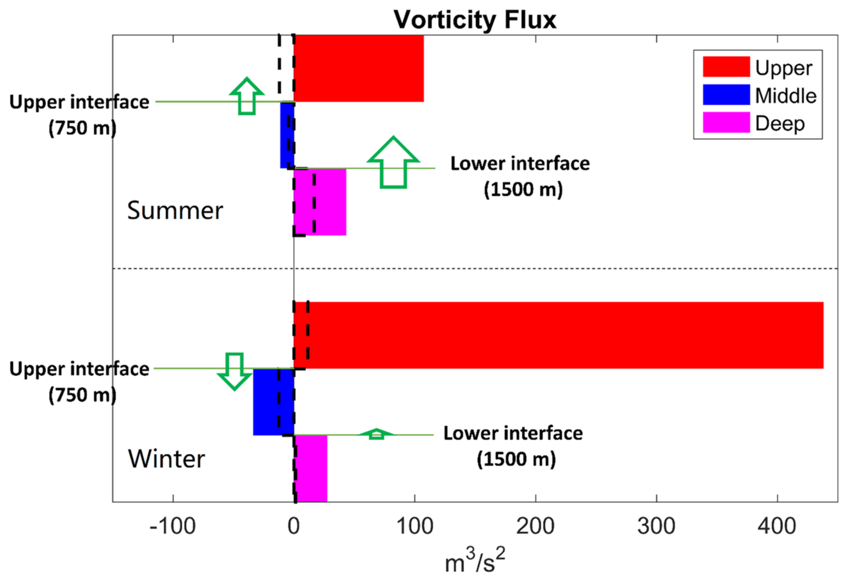

Figure 6. External planetary vorticity flux (m^3/s^2) through LS in the upper, middle, and deep layers during summer and winter. The black dashed box indicates the contribution of vertical vorticity flux in each layer. Green open arrows indicate the upward and downward flux crossing the upper (750 m) and lower (1,500 m) interfaces between adjacent layers.

in the northern part of the basin, where there is larger f, provided a large enough vorticity flux to offset the upward vorticity flux in the south. Thus, the net vertical vorticity flux crossing the lower interface was not important to the basin-scale circulation in the middle and deep layers during winter.

Clearly, during summer, the net vertical vorticity fluxes crossing both upper and lower interfaces had relatively large magnitudes, but during winter, only the net flux crossing the upper interface was important. Because external vorticity flux through several straits was relatively large in the upper layer, the vertical vorticity flux had much significant influence on the circulation in the semi-closed middle and deep layers.

4. Discussion

Based on the momentum balance in steady state, the horizontal velocity can be separated into three components: $-f\vec{k}\times\vec{V}_{h\_geo}=-\frac{1}{\rho_0}\nabla_h P$; $-f\vec{k}\times\vec{V}_{h\_adv}=-\vec{V}\cdot\nabla\vec{V}_h$; $-f\vec{k}\times\vec{V}_{h\_vvis}=\frac{\partial}{\partial z}\left(K_v\frac{\partial\vec{V}_h}{\partial z}\right)$. To explore the contributions of different processes to the VE in the CAC circulation, we separated VE into three parts accordingly: the geostrophic component, VE_{geo}; nonlinear advection component, VE_{adv}; and vertical viscosity component, VE_{vvis}.

$$VE(z)=-\nabla_h\cdot\int_{-H}^{z}\overrightarrow{V_h}\,dz=-\nabla_h\cdot\int_{-H}^{z}\left(\vec{V}_{h\_geo}+\vec{V}_{h\_adv}+\vec{V}_{h\_vvis}\right)dz. \quad (3)$$

The geostrophic balance controls the basic basin circulation, and the ageostrophic component is stronger near LS and MS where the current exchange has strong nonlinearity (Gan et al., 2006; Nan et al., 2011). We thus divided the five regions of the SCS shown in Figure 4 into two groups. The first group was basin Regions B, C, and E, where the strong slope current contributed most to the basin-wide circulation. The second group included Regions A and D under direct influence of external forcing. The total VE and the respective components in these two groups are shown in Figure 7 as a function of depth.

The vertical VE pattern inside the basin was dominated by the geostrophic component with upward/downward motion above/below ~2,000 m in summer and winter (Figures 7a and 7b). In response to the deep/middle layer cyclonic/anticyclonic slope current, the upward VE and VE_{geo} at the upper interface was weaker than the upward VE at the lower interface inside the basin. The influence of the nonlinear

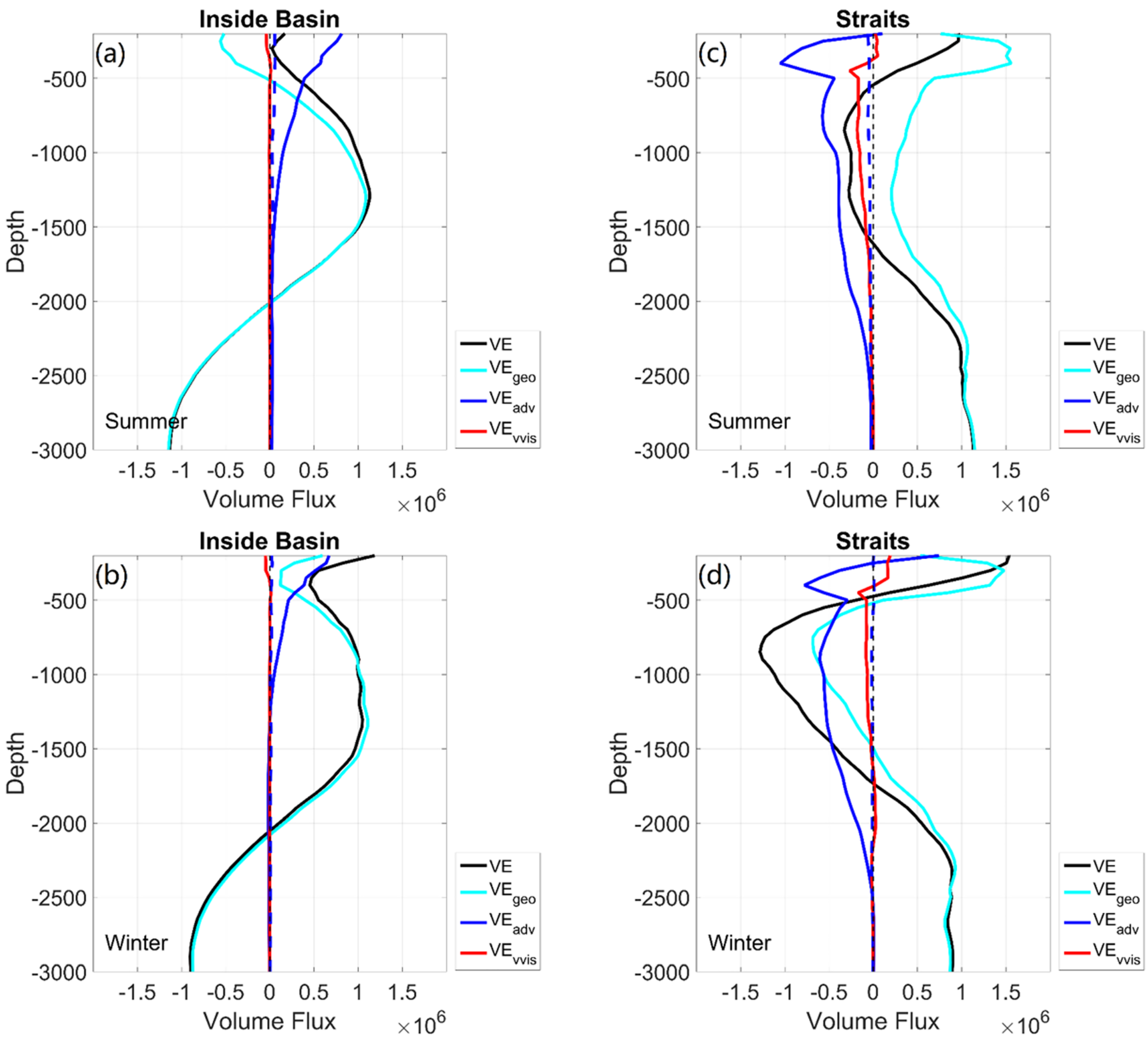

Figure 7. Vertical profiles of VE, VE_{geo}, VE_{adv}, VE_{vvis} (m^3/s) in Equation 3 integrated over regions (a, b) inside the basin and (c, d) near LS and MS during summer and winter.

component (VE_{adv}) on the VE became stronger only within the upper ocean (above ~500 m), and the effect of VE_{vvis} was relatively small.

Near LS and MS (Figures 7c and 7d), VE_{geo} generally leads to upward motion during summer, and it generated downward motion in the upper and middle layers, between 500 and 1,500 m, during winter. Along with the geostrophic component, the ageostrophic VE_{adv} contributed much of the downward VE in the water column, and the contribution of VE_{vvis} was limited. However, the basic vertical variation of VE was still controlled by VE_{geo}.

We focused on VE_{geo} inside the basin, where the slope current contributed most to the basin-wide circulation and linked with the large-scale net VE. The VE_{geo} can be further interpreted as

$$-\nabla_h \cdot \int_{-H}^{z} \left(\overrightarrow{V}_{h\_geo} \right) dz = -\frac{1}{f} \nabla \times \int_{-H}^{z} \overrightarrow{PGF} dz + \frac{\beta}{f} \int_{-H}^{z} v_{geo} dz = -\left(v_{b\_geo} H_y + u_{b\_geo} H_x \right) + \frac{\beta}{f} \int_{-H}^{z} v_{geo} dz. \quad (4)$$

The two terms on the right side of Equation 4 represent the cross-isobath geostrophic transport (CGT_b) at the bottom induced by the along-isobath PGF at the bottom and the beta effect of the meridional geostrophic

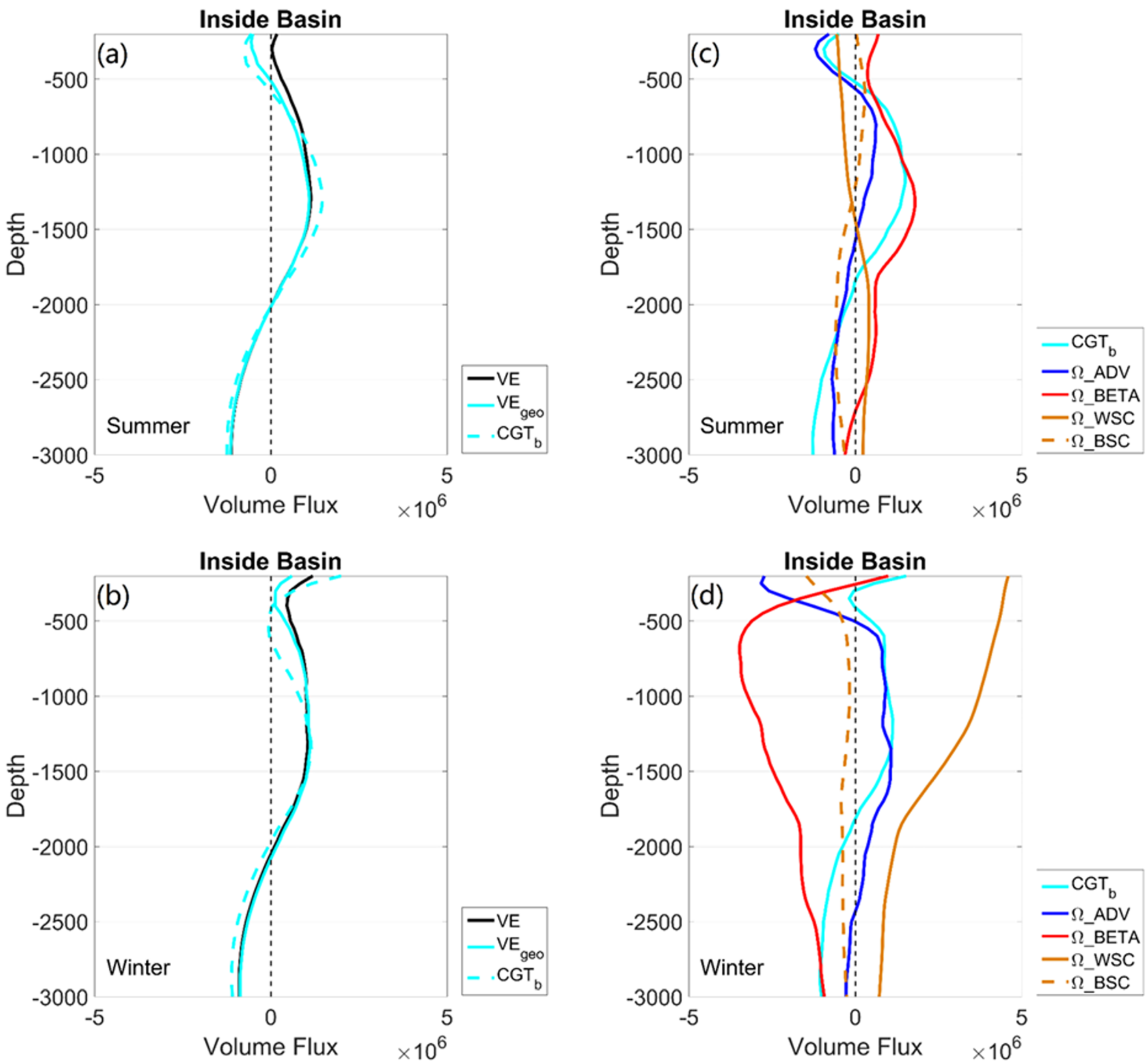

Figure 8. Vertical profiles of VE, VE_{geo}, and CGT_b (m^3/s) integrated over the regions inside the basin during (a) summer and (b) winter. (c, d) Same as (a) and (b), but for the major terms in the depth-integrated vorticity dynamics of Equation 5.

current below depth z. The upslope/downslope CGT_b could generate an upward/downward VE over the slope according to the bottom kinematic boundary condition, which was concurrently modified by the beta effect.

Figures 8a and 8b show that the basic structure of the $VE_{geo}(z)$ integrated inside the basin was chiefly generated by the CGT_b during summer and winter. In the individual region in the basin, the CGT_b also largely controlled the basic region-integrated VE pattern (figures not shown). At the upper interface, the net upslope CGT_b induced the upward VE, which weakened the anticyclonic and cyclonic slope current in the middle and upper layers, respectively. At the lower interface, the upslope geostrophic transport in the deep layer was mainly generated along the meandering deep western slope and over the southern basin, which induced upward motion into the middle layer. Conversely, the upslope CGT_b that crossed the lower interface enhanced the cyclonic and anticyclonic slope current in the deep and middle layers, respectively. The upslope CGT_b crossing the lower interface was stronger than the CGT_b crossing the upper interface, which indicated that the anticyclonic along-slope current in the middle layer formed the downslope CGT_b and offset part of the upward VE coming from the deep layer.

10.1029/2020JC016131

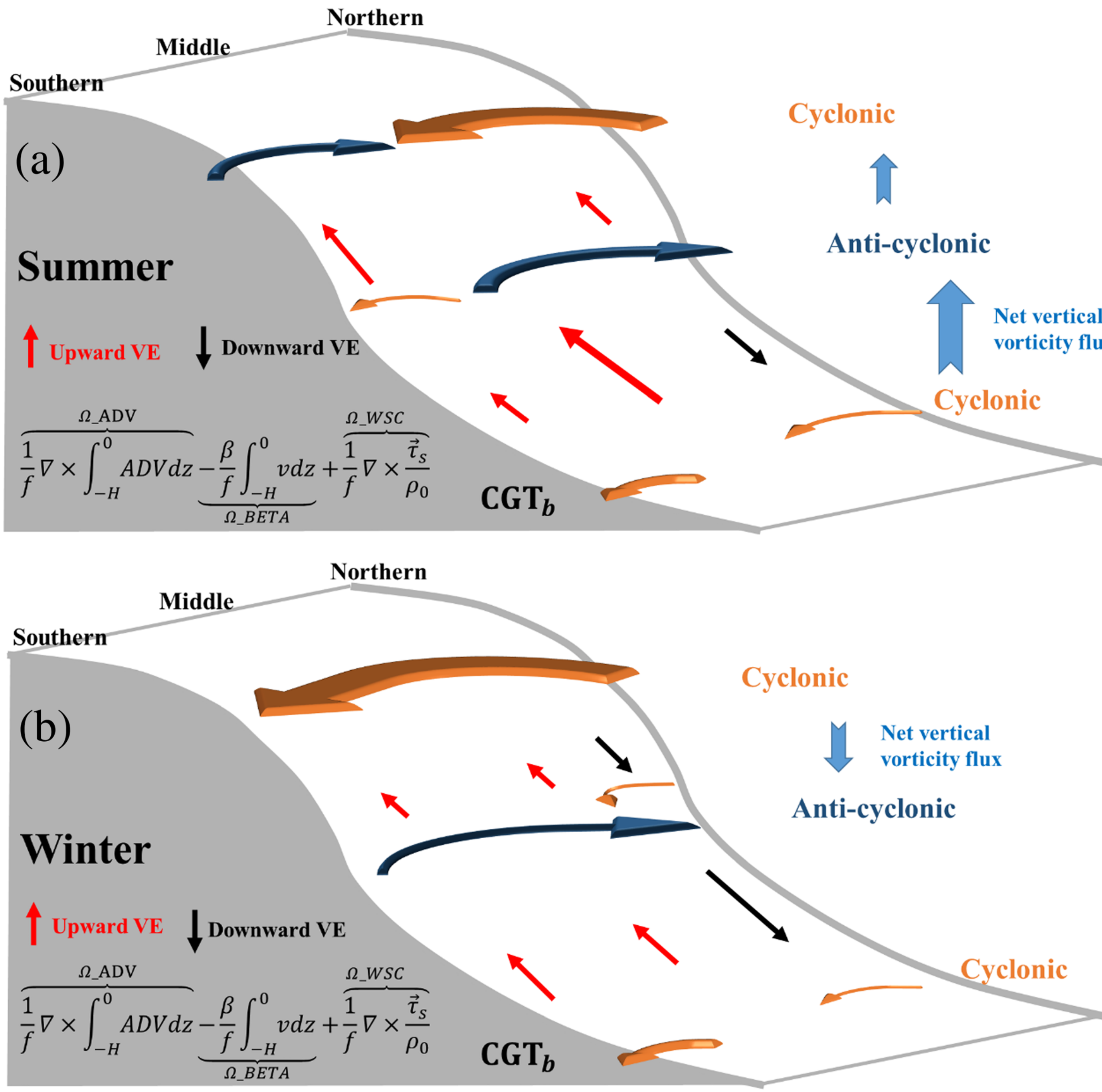

Figure 9. The conceptual schematic figure summarizes the three-dimensional circulation and VE in SCS during (a) summer and (b) winter.

Based on depth-integrated vorticity dynamics (Gan et al., 2013), the formation of CGT_b can be illustrated as

$$CGT_b = -\frac{1}{f}\nabla\times\int_{-H}^{0}\overrightarrow{PGF}dz = \overbrace{\frac{1}{f}\nabla\times\int_{-H}^{0}ADVdz}^{\Omega\_ADV}\underbrace{-\frac{\beta}{f}\int_{-H}^{0}vdz}_{\Omega\_BETA}+\overbrace{\frac{1}{f}\nabla\times\frac{\vec{\tau}_s}{\rho_0}}^{\Omega\_WSC}\underbrace{-\frac{1}{f}\nabla\times\frac{\vec{\tau}_b}{\rho_0}}_{\Omega\_BSC}. \quad (5)$$

The CGT_b is induced by nonlinear advection, the beta effect, surface wind stress curl (WSC), and bottom friction curl, respectively. The curl of the horizontal viscosity is included in the nonlinear advection term for simplicity.

Because $VE_{geo}(z)$ integrated inside the basin was controlled by the CGT_b in the area with depth $>z$ (Figures 7a and 7b), we obtained the respective processes contributing to CGT_b by integrating Equation 5 in the same area. Our results are shown in Figures 8c and 8d. The figures show how CGT_b formed, which largely determined the basic net VE pattern inside the basin. During summer (Figure 8c), the beta effect and nonlinear advection of basin circulation mainly induced the net upslope CGT_b crossing the interfaces. At the upper interface, the beta effect and nonlinear advection contributed to the upslope CGT_b, while the WSC played a negative role. At the lower interface, the contributions of the nonlinear advection and WSC were limited, and the positive beta effect contributed the most to the upslope CGT_b.

During winter (Figure 8d), the formation mechanism of CGT_b inside the basin varied. The WSC and beta effect had larger magnitudes but opposite signs. The magnitude of the nonlinear advection was relatively small but generally had a similar vertical pattern to VE. The joint effect of the WSC, the beta effect, and the nonlinear advection determined the basic vertical pattern of CGT_b and the corresponding VE crossing the lower and upper interfaces. At the upper interface, the intensified winter wind forcing provided positive WSC and the corresponding northward transport in the water column over the interior basin. The positive WSC and negative beta effect induced CGT_b for the upslope and downslope motions, respectively. At the lower interface, the WSC and the beta effect also had opposite signs that offset each other, and the positive nonlinear advection contributed to the CGT_b for upslope motion. Thus, although the magnitude of the positive nonlinear advection was relatively small, it largely determined the intensity of the CGT_b at two interfaces for the net upslope motion.

5. Summary

The coupled dynamics of the external layered fluxes through LS and the internal vertical flux form and sustain a three-layer CAC circulation in the SCS. The internal VE, in response to the external flux, plays an important role in regulating the slope current structure that sustains the basin circulation. Yet we know little about the internal vertical flux in the SCS basin. Using the results from CMOMS, this study investigated the spatiotemporal structure of the internal VE crossing the upper (750 m) and lower (1,500 m) interfaces that separate the CAC circulation into the three layers (Figure 9). We characterized the VE in the CAC circulation, illustrated the vertical coupling between the neighboring layers, and explored the underlying dynamics.

The relatively strong VE occurred mainly over the basin slope, because of the interaction between the slope current and the meandering bottom topography. Additional VE-active region located near the LS under the influence of the external exchanging flows. At the upper interface, there was a net upward transport of 0.50 Sv during summer, which weakened the cyclonic/anticyclonic circulation in the upper/middle layer. The opposite situation occurred during winter when there was a net downward transport of 0.29 Sv. At the lower interface, the VE had relatively large magnitude compared to that across the upper interface. Overall, there was a net upward VE (0.87 Sv in summer and 0.56 Sv in winter) crossing the lower interface, which was stronger during summer due to a larger influx through LS.

The transport of the VE produced vertical vorticity flux in each layer to maintain the CAC circulation, particularly in the semi-closed middle and deep layers. But it had much smaller influences on the upper layer because external vorticity flux through several straits was relatively large. During summer, the prevailing upward vorticity flux crossing the two interfaces induced the net positive/negative vorticity input for the cyclonic/anticyclone circulation in the deep/middle layer, which accounted for ~40% of the total external planetary vorticity flux. During winter, the net downward vertical vorticity flux crossing the upper interface was still equivalent to ~40% of the external planetary vorticity flux in the middle layer. While at the lower interface, the magnitude of the vertical vorticity flux was much smaller than the upper interface.

VE was mainly caused by the CGT_b along the meandering slope in the basin, in response to the external flux through LS and to wind forcing. Generally, the upslope CGT_b from the deep layer along the meandering deep slope induced upward motion across the lower interface inside the basin, predominantly along the western slope where there are a steep slope and strong along-slope current. In contrast, the anticyclonic along-slope current in the middle layer formed the downslope transport and offset part of the upward VE from the deep layer. Near MS and LS, under the direct influence of external forcing, the geostrophic component affected the basic vertical profile pattern of VE, and the nonlinear advection component contributed a great deal to the net downward VE.

Vorticity dynamics revealed that, in summer, the bottom along-isobath pressure gradient that induced CGT_b inside the basin was mainly provided by the beta effect and nonlinear advection of the background basin circulation. The WSC generally had a negative effect. In winter, the WSC and beta effect had opposite signs that offset each other because of the Sverdrup balance, and the nonlinear advection dominated the basic vertical variation pattern of VE.

Data Availability Statement

The data used in this study are derived from China Sea Multi-Scale Ocean Modeling System (CMOMS, https://odmp.ust.hk/cmoms/) based on Regional Ocean Modeling System (https://www.myroms.org/).

Acknowledgments

This research was supported by the Key Research Project of the National Science Foundation of China (41930539), the Theme-based Research Scheme (T21-602/16-R) of the Hong Kong Research Grants Council, and the Hong Kong Research Grants Council (GRF16204915 and GRF16206516). We are also grateful to the support of The National Supercomputing Centers of Tianjin and Guangzhou.

References

Cai, Z., & Gan, J. (2019). Coupled external-internal dynamics of layered circulation in the South China Sea: A modeling study. *Journal of Geophysical Research: Oceans*, *124*, 5039–5053. https://doi.org/10.1029/2019jc014962

Cai, Z., Gan, J., Liu, Z., Rex, H., & Li, J. (2020). Progress on the formation dynamics of the layered circulation in the South China Sea. *Progress in Oceanography*, *181*(202), 102246. https://doi.org/10.1016/j.pocean.2019.102246

Chen, C.-T. A., & Huang, M.-H. (1996). A mid-depth front separating the South China Sea water and the Philippine sea water. *Journal of Oceanography*, *52*(1), 17–25. https://doi.org/10.1007/BF02236530

Fang, G., Wang, Y., Wei, Z., Fang, Y., Qiao, F., & Hu, X. (2009). Interocean circulation and heat and freshwater budgets of the South China Sea based on a numerical model. *Dynamics of Atmospheres and Oceans*, *47*(1), 55–72.

Gan, J., & Allen, J. S. (2002). A modeling study of shelf circulation off northern California in the region of the Coastal Ocean Dynamics Experiment: Response to relaxation of upwelling winds. *Journal of Geophysical Research*, *107*(C9), 3123. https://doi.org/10.1029/2000JC000768

Gan, J., Li, H., Curchitser, E. N., & Haidvogel, D. B. (2006). Modeling South China Sea circulation: Response to seasonal forcing regimes. *Journal of Geophysical Research*, *111*, C06034. https://doi.org/10.1029/2005jc003298

Gan, J., Liu, Z., & Hui, C. R. (2016). A three-layer alternating spinning circulation in the South China Sea. *Journal of Physical Oceanography*, *46*(8), 2309–2315. https://doi.org/10.1175/jpo-d-16-0044.1

Gan, J., Liu, Z., & Liang, L. (2016). Numerical modeling of intrinsically and extrinsically forced seasonal circulation in the China seas: A kinematic study. *Journal of Geophysical Research: Oceans*, *121*, 4697–4715. https://doi.org/10.1002/2016JC011800

Gan, J., & Qu, T. (2008). Coastal jet separation and associated flow variability in the southwest South China Sea. *Deep Sea Research Part I*, *55*(1), 1–19. https://doi.org/10.1016/j.dsr.2007.09.008

Gan, J., San Ho, H., & Liang, L. (2013). Dynamics of intensified downwelling circulation over a widened shelf in the Northeastern South China Sea. *Journal of Physical Oceanography*, *43*(1), 80–94. https://doi.org/10.1175/JPO-D-12-02.1

Hsin, Y.-C., Wu, C.-R., & Chao, S.-Y. (2012). An updated examination of the Luzon Strait transport. *Journal of Geophysical Research*, *117*, C03022. https://doi.org/10.1029/2011jc007714

Katsman, C. A. (2006). Impacts of localized mixing and topography on the stationary abyssal circulation. *Journal of Physical Oceanography*, *36*, 1660–1671. https://doi.org/10.1175/JPO2925.1

Lan, J., Wang, Y., Cui, F., & Zhang, N. (2015). Seasonal variation in the South China Sea deep circulation. *Journal of Geophysical Research: Oceans*, *120*, 1682–1690. https://doi.org/10.1002/2014JC010413

Lan, J., Zhang, N., & Wang, Y. (2013). On the dynamics of the South China Sea deep circulation. *Journal of Geophysical Research: Oceans*, *118*, 1206–1210. https://doi.org/10.1002/jgrc.20104

Liang, X., Spall, M., & Wunsch, C. (2017). Global ocean vertical velocity from a dynamically consistent ocean state estimate. *Journal of Geophysical Research: Oceans*, *122*, 8208–8224. https://doi.org/10.1002/2017JC012985

Liu, Z., & Gan, J. (2017). Three-dimensional pathways of water masses in the South China Sea: A modeling study. *Journal of Geophysical Research: Oceans*, *122*, 6039–6054. https://doi.org/10.1002/2016JC012511

Liu, Z. Q., & Gan, J. P. (2016). Open boundary conditions for tidally and subtidally forced circulation in a limited-area coastal model using the Regional Ocean Modeling System (ROMS). *Journal of Geophysical Research: Oceans*, *121*, 6184–6203. https://doi.org/10.1002/2016JC011975

Luyten, J., & Stommel, H. (1986). Gyres driven by combined wind and buoyancy flux. *Journal of Physical Oceanography*, *16*(9), 1551–1560. https://doi.org/10.1175/1520-0485(1986)016<1551:GDBCWA>2.0.CO;2

Marchal, O., & Nycander, J. (2004). Nonuniform upwelling in a shallow-water model of the Antarctic bottom water in the Brazil Basin. *Journal of Physical Oceanography*, *34*(11), 2492–2513. https://doi.org/10.1175/JPO2643.1

Masumoto, Y., Sasaki, H., Kagimoto, T., Komori, N., Ishida, A., Sasai, Y., et al. (2004). A fifty-year eddy-resolving simulation of the world ocean–preliminary outcomes of OFES (OGCM for the earth simulator). *J. Earth Simulator*, *1*, 35–56.

Nan, F., Xue, H., Xiu, P., Chai, F., Shi, M., & Guo, P. (2011). Oceanic eddy formation and propagation southwest of Taiwan. *Journal of Geophysical Research*, *116*, C12045. https://doi.org/10.1029/2011jc007386

Qu, T. (2000). Upper-layer circulation in the South China Sea. *Journal of Physical Oceanography*, *30*(6), 1450–1460. https://doi.org/10.1175/1520-0485(2000)030<1450:ULCITS>2.0.CO;2

Qu, T., Song, Y. T., & Yamagata, T. (2009). An introduction to the South China Sea throughflow: Its dynamics, variability, and application for climate. *Dynamics of Atmospheres and Oceans*, *47*(1-3), 3–14. https://doi.org/10.1016/j.dynatmoce.2008.05.001

Quan, Q., & Xue, H. (2018). Layered model and insights into the vertical coupling of the South China Sea circulation in the upper and middle layers. *Ocean Modelling*, *129*, 75–92. https://doi.org/10.1016/j.ocemod.2018.06.006

Shchepetkin, A. F., & McWilliams, J. C. (2005). The Regional Ocean Modeling system: A split-explicit, free-surface, topography following coordinates ocean model. *Ocean Modell.*, *9*(4), 347–404. https://doi.org/10.1016/j.ocemod.2004.08.002

Song, Y. T., & Chao, Y. (2004). A theoretical study of topographic effects on coastal upwelling and cross-shore exchange. *Ocean Modell*, *6*(2), 151–176. https://doi.org/10.1016/S1463-5003(02)00064-1

Stommel, H., & Arons, A. B. (1960). On the abyssal circulation of the World Ocean. Part I: stationary planetary flow patterns on a sphere. *Deep Sea Research*, *6*, 140–154.

Su, J. L. (2004). Overview of the South China Sea circulation and its influence on the coastal physical oceanography outside the Pearl River estuary. *Continental Shelf Research*, *24*(16), 1745–1760. https://doi.org/10.1016/j.csr.2004.06.005

Tian, J., Yang, Q., Liang, X., Xie, L., Hu, D., Wang, F., & Qu, T. (2006). Observation of Luzon Strait transport. *Geophysical Research Letters*, *33*, L19607. https://doi.org/10.1029/2006GL026272

Wang, A., Du, Y., Peng, S., Liu, K., & Huang, R. X. (2018). Deep water characteristics and circulation in the South China Sea. *Deep Sea Research Part I: Oceanographic Research Papers*, *134*, 55–63. https://doi.org/10.1016/j.dsr.2018.02.003

Wang, G., Huang, R. X., Su, J., & Chen, D. (2012). The effects of thermohaline circulation on wind-driven circulation in the South China Sea. *Journal of Physical Oceanography*, *42*(12), 2283–2296. https://doi.org/10.1175/JPO-D-11-0227.1

Wang, G., Xie, S. P., Qu, T., & Huang, R. X. (2011). Deep South China Sea circulation. *Geophysical Research Letters*, *38*, L05601. https://doi.org/10.1029/2010GL046626

Xu, F.-H., & Oey, L.-Y. (2014). State analysis using the local ensemble transform Kalman filter (LETKF) and the three-layer circulation structure of the Luzon Strait and the South China Sea. *Ocean Dynamics*, *64*(6), 905–923. https://doi.org/10.1007/s10236-014-0720-y

Xue, H., Chai, F., Pettigrew, N., Xu, D., Shi, M., & Xu, J. (2004). Kuroshio intrusion and the circulation in the South China Sea. *Journal of Geophysical Research*, *109*, C02017. https://doi.org/10.1029/2002JC001724

Yang, J., & Price, J. F. (2000). Water-mass formation and potential vorticity balance in an abyssal ocean circulation. *Journal of Marine Research*, *58*(5), 789–808. https://doi.org/10.1357/002224000321358918

Yang, J., & Price, J. F. (2007). Potential vorticity constraint on the flow between two basins. *Journal of Physical Oceanography*, *37*(9), 2251–2266. https://doi.org/10.1175/JPO3116.1

Yuan, D. (2002). A numerical study of the South China Sea deep circulation and its relation to the Luzon Strait transport. *Acta Oceanologica Sinica*, *21*(2), 187–202.

Zhu, Y., Sun, J., Wang, Y., Li, S., Xu, T., Wei, Z., & Qu, T. (2019). Overview of the multi-layer circulation in the South China Sea. *Progress in Oceanography*, *175*, 171–182. https://doi.org/10.1016/j.pocean.2019.04.001

Zhu, Y., Sun, J., Wang, Y., Wei, Z., Yang, D., & Qu, T. (2017). Effect of potential vorticity flux on the circulation in the South China Sea. *Journal of Geophysical Research: Oceans*, *122*, 6454–6469. https://doi.org/10.1002/2016jc012375